Version of Record: https://www.sciencedirect.com/science/article/pii/S135964621930171X
Manuscript_c5a153bc6a6891cee0eb98b48077361e

Corrosion-resistant high entropy alloy with high strength and ductility

S.S. Nene[1], M. Frank[1], K. Liu[1], S. Sinha[1], R.S. Mishra[1*], B.A. McWilliams[2], K.C. Cho[2]

[1]*Center for Friction Stir Processing, Department of Materials Science and Engineering, University of North Texas, Denton, Texas 76207 USA*

[2]*Weapons and Materials Research Directorate, U.S. Army Research Laboratory, Aberdeen Proving Grounds, MD 21005 USA*

**Corresponding author email: Rajiv.Mishra@unt.edu*

Abstract

High-strength materials lack a synergistic combination of mechanical properties and corrosion resistance desired for most structural applications. Phase and grain boundary architecturing is done in the material to attain balance in these properties. A friction stir processed $Fe_{38.5}Mn_{20}Co_{20}Cr_{15}Si_5Cu_{1.5}$ (Cu-HEA) exhibited excellent mechanical properties and high corrosion resistance in synergy. The excellent mechanical properties were attributed to the controlled transformation of ultrafine γ matrix and ε twinning; whereas good corrosion resistance was due to homogenized fine grained γ microstructure. In short, Cu-HEA design opens a new pathway towards realizing strong and ductile alloys with tunable corrosion resistance by engineering matrix metastability.

Key words: high entropy alloy (HEA); Cu-HEAs; corrosion resistance; TRIP stress

Advanced structural steels and titanium alloys are known for their useful mechanical properties, whereas stainless steels and Ni base alloys demonstrate steady corrosion resistance. The strength-ductility combination of most of these materials is reliable even though the materials fail to survive for longer durations in corrosive media such as sea water [1, 2]. This failure to survive is attributed mainly to the contrasting response of grain boundaries and second-phase particles to deformation and corrosion phenomena [1–3]. Increase in grain boundary area enhances the material's ability to store deformation, thereby increasing its strength and ductility; whereas more grain boundaries/second phase particles can form a network of galvanic cells among the matrix and themselves, thereby lowering corrosion resistance [1–3].

© 2019 published by Elsevier. This manuscript is made available under the Elsevier user license
https://www.elsevier.com/open-access/userlicense/1.0/

Design of high entropy alloys opened a new compositional domain for exploration wherein recently-designed $Al_xCoCrFeNi$ HEAs confirmed the genuine potential of corrosion resistance in chloride medium; but, again, at the expense of limited ductility compared with the transformation-assisted $Fe_{50}Mn_{30}Co_{10}Cr_{10}$ HEA (DP-HEA) [4–6]. This sets a strong foundation for the design of new materials that can exhibit reliable mechanical properties without losing resistivity to atmospheric conditions. This paper thus demonstrates the design and processing strategy to attain not only exceptional work hardening ability but also to retain structural character to prevent localized galvanic attack in a corrosive medium [7–10]. Such work hardening ability and structural character were realized by the friction stir processing (FSP) of Fe-Mn-Co-Cr-Si containing HEA having 1.5 at% Cu. Cu is known to have low solid solubility in most of these matrix elements and hence should form a Cu-rich second phase; whereas if it is dissolved, γ matrix stability is increased [7-10].

$Fe_{38.5}Mn_{20}Co_{20}Cr_{15}Si_5Cu_{1.5}$ (Cu-HEA, (at %)) HEA was produced by vacuum arc-casting in a cold-copper crucible. The vacuum level achieved was approximately 300 μm, and the chamber was backfilled with argon to 1 atm prior to each melt, using pure metals to ingot dimensions of 300×100×6 mm^3. Subsequently, these 6 mm thick sheets were friction stir processed using a W-Re tool with the parameters shown in Table 1. Double pass (D-pass) processing essentially involves two overlapping friction stir processing (FSP) runs, starting with a 350 rotations per minute (RPM) run followed by an overlapping run at 150 RPM. A Cu backing plate was used for effective heat dissipation, and Ar was blown near the specimen tool interface to avoid oxygen pickup during processing. The processing tool had a shoulder diameter of 12 mm with a tapered pin. The root diameter, pin diameter, and length of the tool were 7.5 mm, 6 mm, and 3.5 mm, respectively.

Microstructures of the alloy in as-cast (coarse-grained) and as-FSP (grain-refined) conditions were analyzed by Electron backscatter diffraction (EBSD) measurements carried out on FEI NOVA Nano (SEM) with a Hikari camera, and the data were analyzed using TSL OIM 8 software. The coarse-grained HEA EBSD was done at a magnification of 600 X with step size 0.8 μm and area 273 × 218 μm^2. As the grain size attained during FSP was significantly fine, EBSD scans were at magnifications 2000 X and 6000 X. To capture sufficient grains during high magnification scans (6000 X), grain size and phase fractions were estimated at three different locations, and the average values have been reported.

Rectangular 1 mm-thick, dog-bone-shaped mini-tensile specimens were machined using a computer numerical control (CNC) machine from 1 mm below the surface within the nugget region of all FSP specimens; whereas specimens for as-cast condition were machined from the top surface of the as-cast ingot. Gage length and width of the tensile specimens were 5 and 1.25 mm, respectively. In each condition, three samples were tested at room temperature and initial strain rate of 10^{-3} s^{-1} to confirm reproducibility of the results. Electro-chemical studies were conducted in 3.5 wt.% NaCl solution at least three times to confirm repeatability of results. Potentiodynamic polarization scans were made with scan rate of 0.166 mV/s. All electrochemical measurements used saturated calomel electrode (SCE) as reference electrode and platinum as counter electrode.

Fig. 1a shows the effect of Cu addition on phase evolution by thermodynamic calculations. The phase diagram calculated for $Fe_{40-X}Mn_{20}Co_{20}Cr_{15}Si_5Cu_X$ depicts clear dual phase (f.c.c. + f.c.c.) regions above ~350°C and below which γ-dominated (γ+ε) phase field for $Fe_{38.5}Mn_{20}Co_{20}Cr_{15}Si_5Cu_{1.5}$ forms (Cu-HEA marked by red dotted line in (Fig. 1 (a)). Figures 1 (b)–(d) capture overall microstructural evolution in the EBSD phase maps upon FSP of as-cast Cu-HEA (Fig. 2 (b)). Irrespective of processing condition, γ phase was stabilized after FSP with minor

traces of ε phase. γ phase dominance upon FSP is a strong indicator of intrinsic increase in γ stability due to Cu addition compared to stability of γ phase in CS-HEA [11]. Of interest is that single-pass processing led to almost equiaxed microstructures with different extents of grain refinement (Figs. 2 (c), (d)). However, double pass (D-pass) processing led to biomodal microstructural evolution (Fig. 2 (e)) having regions of very fine grains surrounded by big grains [12–13]. Figs. 2 e_1 and e_2 display the EBSD image quality (IQ) and grain size distribution maps respectively which also clearly supports the bimodal nature of microstructure.

This bimodal grain evolution is the result of Cu precipitation from the Cu-rich regions (region A_1 shown in Fig. 1e_1) in the matrix and pins the grain boundaries from further grain growth. The highlighted region marked with yellow arrows in Fig. 1e_1 confirms that these Cu precipitates are very fine and form near the grain boundaries. The presence of Cu rich and depleted (region A_2 shown in Fig. 1e_1) regions are also in accordance with the two distinct f.c.c. dominated phase field predicated by Thermo-Calc in Fig. 1a. An EDS elemental distribution (Fig. 1e_3) away from the fine-grained region showed depletion of the Cu (Fig. 1 e_3) and supports the fact that this abnormal grain refinement occurred in Cu-rich regions only. Hence, being bimodal, D-pass microstructure should show highest yield strength and ductility among all FSP conditions, and indeed is evident from engineering stress-strain curves (Fig. 2 a). As a result, the ability of finer grains to provide Hall-Petch strengthening whereas higher work hardening ability given by relatively coarser grains provides the good combination of yield strength and ductility to D-pass specimen [13–14].

Figure 2 (b) presents conventional Hall-Petch fitting (black line in Fig. 2b) for the grain refined Cu-HEA and highlights the substantial contribution of grain boundary strengthening occurring in the material with grain refinement. Pronounced transformation of either coarser or refined γ matrix to ε phase under deformation makes substantial contribution of transformation-

induced-plasticity (TRIP) [8–10, 15]. Fig. 2c shows the variation of the true stress with WH rate for Cu-HEA as a function of processing condition whereas Figs. 2d-d_3 and 2e-e_3 capture the overall deformation accommodation in as-cast and D-pass specimens with the help of EBSD phase, inverse pole figures (IPF) and geometrically necessary dislocations (GND) density maps, respectively. It is important to note that as-cast material itself showed very high ductility in comparison with as-cast TRIP HEAs we reported earlier [9,10,12]. The evidence of twinning in ε phase supports this higher strain accommodation in as-cast material with uniform GND distribution within ε twins (Fig. 2d_4).

The UTS improved significantly with the grain refinement upon FSP while maintaining ductility in comparison with as-cast condition (Fig. 2a,c). This increased UTS is attributed to the higher WH ability due to pronounced TRIP effect in grain refined FSP Cu-HEA showing almost 83% increase in ε phase fraction upon failure in the D-pass specimen as against 29% in the as-cast condition. Increase in the extent of γ transformation with the finer grain size suggest that the stress required to activate γ→ε transformation is substantially higher in Cu-HEA and can be attained only with fine grain size. As a result, coarse-grained as-cast material showed very limited TRIP (change in color in Figs. 2d-d_1), with some ε twinning. A similar trend from work hardening curves exhibited the lowest stress value for the as-cast condition and the highest stress value for D-pass specimens for the change of slope in the WH curve at a same strain level of ~ 10% (marked by black arrows in Fig. 2 (c)). The magnitude of stress at the onset of change in slope (TRIP stress) in the WH curve is an indication of stress required for altering the deformation modes from slip to non-slip (i.e. transformation in the present work) thereby resulting in sustained WH activity in the material. TRIP stress for a given prior ε fraction at a fixed strain level (~ 10%) is also plotted as a function of grain size (blue line in Fig. 2b) for all Cu-HEA conditions and it shows the Hall-petch

type relation suggesting the fact that, increase in γ grain boundary area due to FSP made it stronger and the TRIP become stress dependent. Therefore, increased γ stability by Cu addition elevated the amount of stress required for ε formation during deformation and hence unlike all other TRIP steels/ HEAs, fine grained D-pass specimen showed extensive TRIP than coarse grained as-cast Cu-HEA specimen [8–10, 15–17].

Figure 3 elaborates the corrosion behavior of Cu-HEA in 3.5 wt.% NaCl solution. Substantial variation in corrosion potential appeared with processing condition and with refinement in grain size, when the alloy became nobler (Fig. 3 (a)). A detailed investigation of surface morphology for as-cast and D-pass specimens after corrosion is shown in Figs. 3 (b)–(e_2). Localized pitting was the main degradation mechanism in Cu-HEA in the presence of a chloride medium (Fig. 3 (b)) in both coarse and fine grained states. The size of the pits was non-uniform, and preferential growth of pits is evident at certain locations. Qio *et al.* [7] reported that Cu addition to CCAs localize the corrosion tendency owing to Cu-assisted segregation in as-cast and by precipitation in as-processed materials. Similar observations for the as-cast condition in the present work thereby show very low E_{corr} and I_{corr} values. This is because as-cast specimen showed Cu and Mn rich phase separation during casting thereby confirming some Cu segregation as shown in Fig. 3b-b_3. Secondary electron imaging of the corrosion pitting for as-cast specimen displayed preferential attack at these Cu-Mn rich phases as shown in the inset of Fig. 3c.

With FSP, Cu was more dissolved in the matrix due to shear and temperature-driven transport [18], and thus the alloy was significantly homogenized and thus became nobler as compared to the as-cast condition. This was confirmed by the substantial decrease in the number of pits formed on the surface of D-pass specimen than as-cast specimen shown in Fig. 3c,d. However, pitting in D-pass specimen is attributed to the presence of Cu-rich regions shown in Fig.

$2e_1$ which got preferentially attacked causing dissolution of Cu-rich phases (Fig. 3 (e_1,e_2,f,g). However, these regions were very limited and the Cu rich phases being extremely small, the pitting tendency got significantly suppressed in D-pass specimen (Fig. 3c,d). The lack of substantial variation in corrosion current density with decrease in grain size suggests that grain boundaries were not attacked selectively during corrosion; rather, Cu partitioning decided corrosion behavior.

Regarding corrosion kinetics, the anodic region showing steeper slope in Fig. $3a_1$ for the as-cast condition than the as-FSP conditions suggests faster corrosion in the former. Higher anodic slope (tending parallel to voltage axis) indicates a tendency of passivation for as-FSP conditions (Fig. 3 (a_1)). However, due to very small regions of Cu-rich and depleted matrix, the passive layer forms and breaks and thus results in metastable passivation [3, 7]. The tendency of metastable passivation can be hindered by reducing Cu rich phase separation thereby avoiding easy breakage and reformation of the passivation layer in grain refined Cu-HEA. Thus, minimizing Cu partitioning either by complete dissolution or by uniform precipitation in the matrix along with grain refinement could make the corrosion more uniform thermodynamically and kinetically.

Figure 4 (a) compares YS and total elongation of advanced TRIP steels [19–23] and leading TRIP and TWIP HEAs [7–10, 17, 24–28], whereas Fig. 4 (b) compares corrosion current and the corrosion potential of some leading HEAs in 3.5 wt.% NaCl. Cu-HEA showed not only an optimal combination of YS and ductility but it also falls within the corrosion-resistant stainless domain on the corrosion current density-potential plot. Interestingly, it outerforms DP-HEA in YS-ductility combination (rightward, half-filled yellow triangle and blue-shaded circle in Fig. 4 (a)); whereas it is better the PH stainless steel in corrosion rate (half-filled pink circle and grey diamond in Fig. 4 (b)). These results indicate that Cu-HEA has a strong potential of exhibiting good mechanical properties without sacrificing corrosion resistance as compared with its leading counterparts. Our

recent work [11] on fatigue behavior of Cu-HEA showed extremely high fatigue resistance due to delayed yet sustained work hardening during crack propagation, thereby overcoming the conventional fatigue failure tendency of ultrafine-grained materials. In short, Cu-HEA exhibited exceptional mechanical properties, good corrosion resistance [11] and very high fatigue resistance synergistically.

In summary, addition of Cu not only increased γ matrix stability but also made it stronger and tougher. Grain refinement of γ matrix enabled to increase the stress for triggering ε formation and hence delayed the TRIP effect during deformation. A delayed but sustained TRIP effect led to very high strength without compromising ductility even with high yield strength. Minimization of Cu partitioning within the γ matrix by FSP would make the alloy more corrosion-resistant thermodynamically and kinetically.

Acknowledgments

The work was performed under a cooperative agreement between the Army Research Laboratory and the University of North Texas (W911NF-19-2-0011). The authors are thankful to the Materials Research Facility for providing access to the microscopy facilities at the University of North Texas.

Declaration of interests: None

References

[1] H. Nakagawa, T. Miyazaki, H. Yokota.,J. Mater. Sci. 35 (2000) 2245.

[2] M.T. Jia , D.L. Zhang, B. Gabbitas, J.M. Liang, C. Kong, Scripta Mater.107(2015)10.

[3] S. L. Assis, S.Wolynec, I. Costa, Elec. Acta 51(2006)1815.

[4] Y. Zhang , T. T. Zuo, Z. Tang, M. C. Gao, K. A. Dahmen, P. K. Liaw, Z.P. Lu, Prog. Mater. Sci. 61(2014)1.

[5] Y.Shi, B. Yang, X. Xie, J. Brechtl, K. A.Dahmen, P.K. Liaw, Corr. Sci. 119 (2017) 33.

[6] H. Luo, Z. Li, A.M. Mingers, D. Raabe, Corr. Sci. 134 (2018) 131.

[7] Y. Qio,S. Thomas,M.A. Gibson, H.L. Fraser, N. Birbilis, Mater. Degdn. 1 (2017) 15.

[8] J.W. Yeh, S.K. Chen, S.J. Lin, J.Y. Gan, T.S. Chin, T.T. Shun, C.H. Tsau, S.Y. Chang, Adv. Eng. Mater. 6(2004)299.

[9] S.S. Nene, K. Liu, M. Frank, R.S. Mishra, B. A. McWilliams, K. C. Cho, Sci. Rep. 8 (2018) 9920.

[10] S.S. Nene, M. Frank, S. Sinha, K. Liu, R.S. Mishra, B. A. McWilliams, K. C. Cho, submitted for publication (2018).

[11] K. Liu, S.S. Nene, M. Frank, S. Sinha, K.Liu, R.S. Mishra, sumitted for publication (2018).

[12] S.S. Nene, M. Frank, K. Liu, S. Sinha, R.S. Mishra, B. A. McWilliams, K. C. Cho, Scripta Mater. 154 (2018) 163.

[13] S. Patra, Sk. Md. Hasan, N. Narasaiah, D. Chakrabarti, Mater. Sci. Eng A 538 (2012) 145.

[14] Z.C. Cordero, B.E. Knight, C.A. Schuh, Intl. Mater. Rev. 61 (2015) 495.

[15] E.I. Galindo-Nava, P.E.J. Castillo, Acta Mater. 128 (2017) 120.

[16] S.S. Nene, K. Liu, M. Frank, R.S. Mishra, R.E. Brennan, K. Cho, Z. Li, D. Raabe, Sci. Rep. 7 (2017) 16167.

[17] M. Wang, Z. Li,D. Raabe, Acta Mater. 147 (2018) 236.

[18] Z. Li, C.C. Tasan, K.G. Pradeep, D. Raabe, Acta Mater. 131 (2017) 323.

[19] S. Palanivel, A. Arora, K.J. Doherty, R.S. Mishra, Mater. Sci. Eng. A 678 (2016) 308.

[20] P. Escobar, D. Silva, D.S. Ferreira, D. Santos, J. Mater. Res. Technol. 4 (2015) 162.

[21] M. Mukherjee, O.N. Mohanty, S. Hashimoto, T. Hojo, K. Sugimoto, ISIJ Intl. 46 (2006) 316.

[22] B.B. He, B.M. Huang, S.H. He,Y. Qi, H.W. Yen, M.X. Huang, Mater. Sci. Eng. A 724 (2018) 11.

[23] D. Raabe, D. Ponge, O. Dmitrieva, D. Sander, Nanoprecipitate-hardened 1.5 GPa steels with unexpected high ductility, Scripta Mater. 60 (2009)1141.

[24] H.W. Yen, S.W. Ooi, M. Eizadjou, A. Breen, C. Y.Huang, H.K.D.H. Bhadeshia, S.P. Ringer, Acta Mater. 82 (2015) 100.

[25] I.S. Wani, T. Bhattacharjee, S. Sheikh, Y.P. Lu, S. Chatterjee, P. Bhattacharjee, S. Guo, N. Tsuji, Ultrafine-grained $AlCoCrFeNi_{2.1}$ eutectic high-entropy alloy, Mater. Res. Let. 4 (2016) 174.

[26] Z.Fu, B.E. MacDonald, Z. Li, Z. Jiang, W. Chen, Y. Zhou, E.J. Lavernia, Mater. Res. Let. 6 (2018) 630.

[27] J.B. Seol, J.W. Bae, Z. Li, J. C. Han, J. G. Kim, D. Raabe, H.S. Kim, Acta Mater. 151 (2018) 366.

[28] S.S. Nene, S. Sinha, M. Frank, K. Liu, R.S. Mishra, B. A. McWilliams, K. C. Cho, App. Mater. Today 13 (2018) 198.

Figures

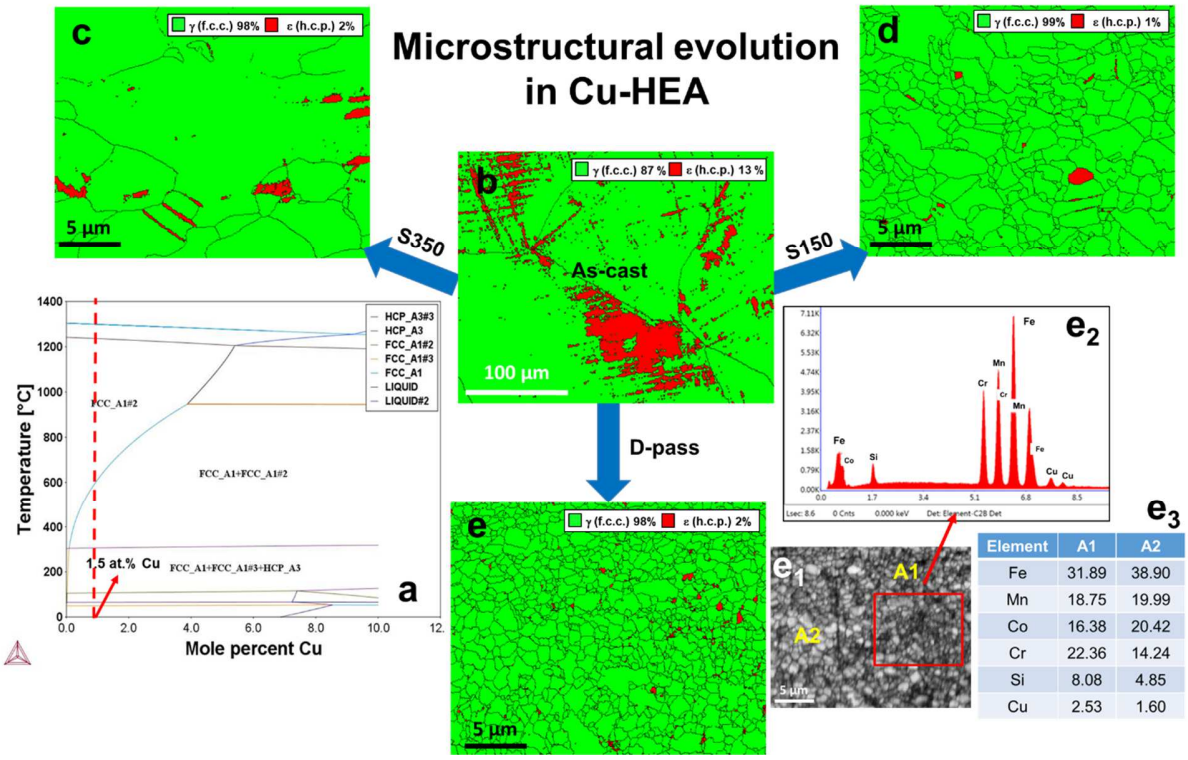

Element	A1	A2
Fe	31.89	38.90
Mn	18.75	19.99
Co	16.38	20.42
Cr	22.36	14.24
Si	8.08	4.85
Cu	2.53	1.60

Figure 1: Microstructural evolution in Cu-HEA: (a) $Fe_{40-X}Mn_{20}Co_{20}Cr_{15}Si_5Cu_X$ phase diagram with TCFE9 database, EBSD phase maps highlighted with HAGB for (b) as-cast, (c) S350, (d) S150, and (e) D-pass conditions. (e_1-e_3) EDS scans for D-pass condition showing Cu-rich and Cu-depleted regions. (EBSD: electron backscattered diffraction: EDS: energy dispersive spectroscopy; HAGB: high angle grain boundaries).

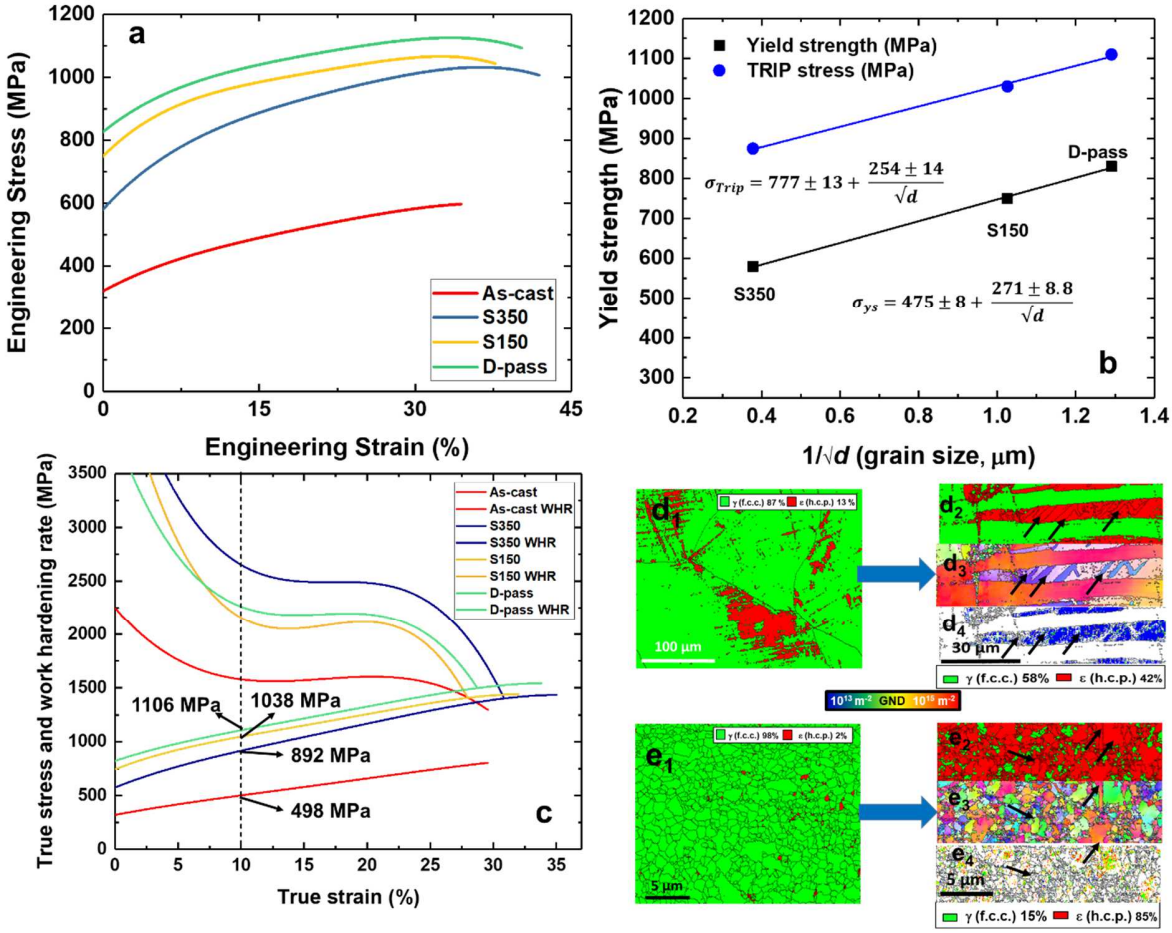

Figure 2: Tensile behavior and deformation mechanisms in Cu-HEA: (a) Engineering stress-strain curves for all as-cast and as-FSP conditions, (b) Hall-Petch relationship plots for Cu-HEA, (c) true stress and work hardening rate vs. true strain, (d_1) EBSD phase map for as-cast condition, (d_2) phase map (d_3) IPF map and (d_4) GND density map for as-cast condition after tensile deformation, (e_1) EBSD phase map for D-pass condition, (e_2) Phase map (e_3) IPF map and (e_4) GND density map for D-pass condition after tensile deformation. (EBSD: electron backscattered diffraction: IPF: inverse pole figure; GND: geometrically necessary dislocations).

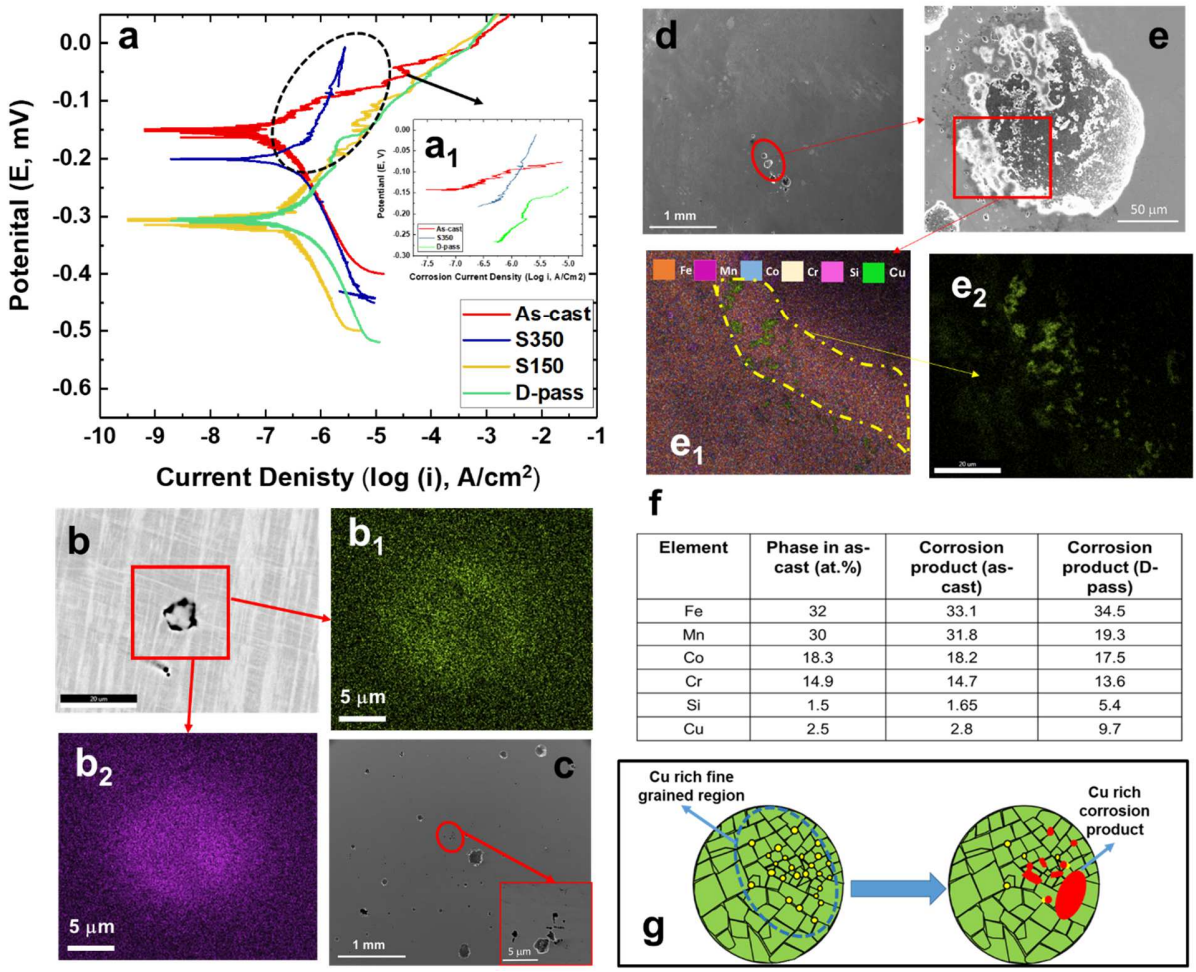

Figure 3: Corrosion behavior of Cu-HEA: (a) Tafel polarization plots for as-cast and as-FSP conditions in 3.5 wt.% NaCl solution, (b) secondary electron image capturing the Cu-Mn rich phase in as-cast specimen, (b_1-b_2) EDS X-ray maps for as-cast specimen showing Cu and Mn rich region, (c) secondary electron image capturing the corrosion pits in as-cast specimen (inset: pitting near the Cu-Mn rich phase), (d) secondary electron image capturing the corrosion pits in D-pass specimen (d_1–d_2) EDS X-ray mapping capturing the Cu-richness in corrosion product and (f) EDS elemental mapping for Cu-Mn rich phase in as-cast condition along with elemental distribution in corrosion products for both the conditions. (g) Schematic showing corrosion attack on Cu rich region in Cl^- medium. (EDS: energy dispersive spectroscopy).

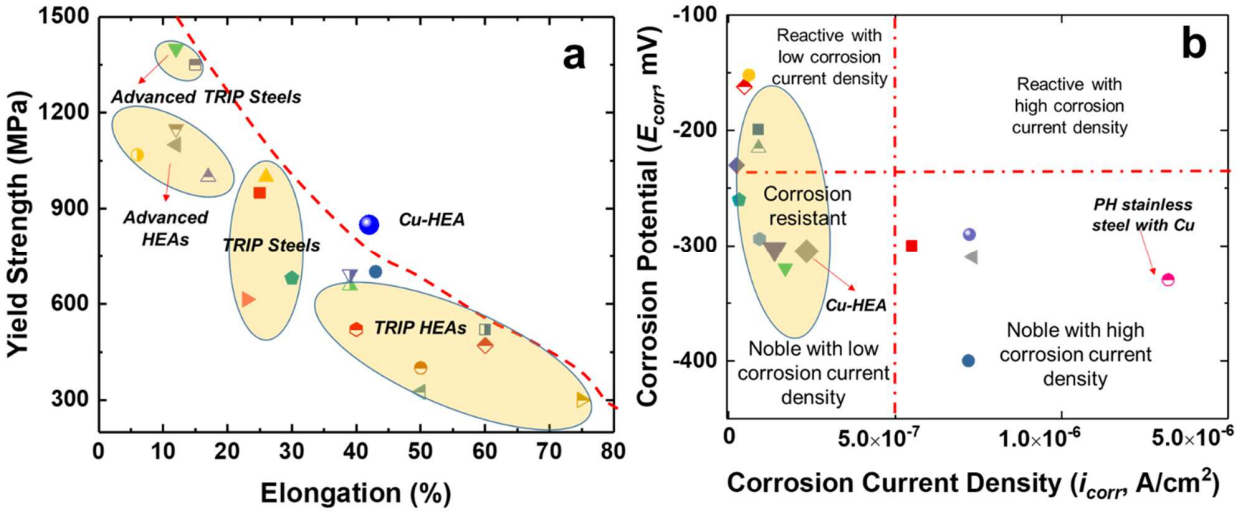

Figure. 4: (a) Yield strength vs. total elongation for advanced TRIP steels and HEAs, (b) Corrosion current density vs. corrosion potential plot for leading HEAs designed so far in comparison with PH-stainless steel [7–10, 17, 19–28].

Table 1: Processing parameters selected for FSP.

Processing parameters	**S350**	**S150**	**D-pass**	
	Single pass	**Single pass**	**Pass 1**	**Pass 2**
Rotational Rate (RPM)	350	150	350	150
Traverse Speed (mm/min)	50.8	50.8	50.8	50.8
Plunge Depth (mm)	3.65	3.65	3.65	3.65
Tilt Angle (°)	2.0	2.0	2.0	2.0

Strong, ductile and corrosion resistant high entropy alloy

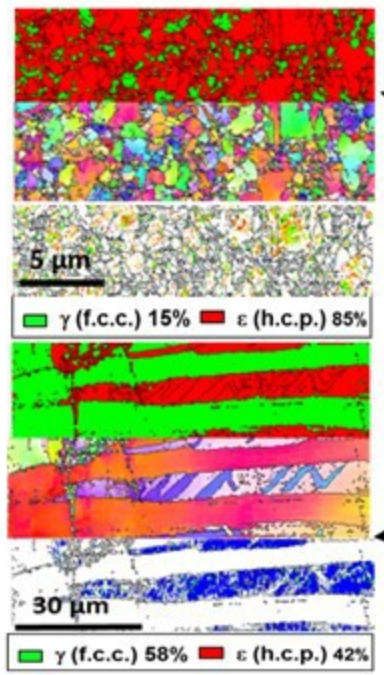

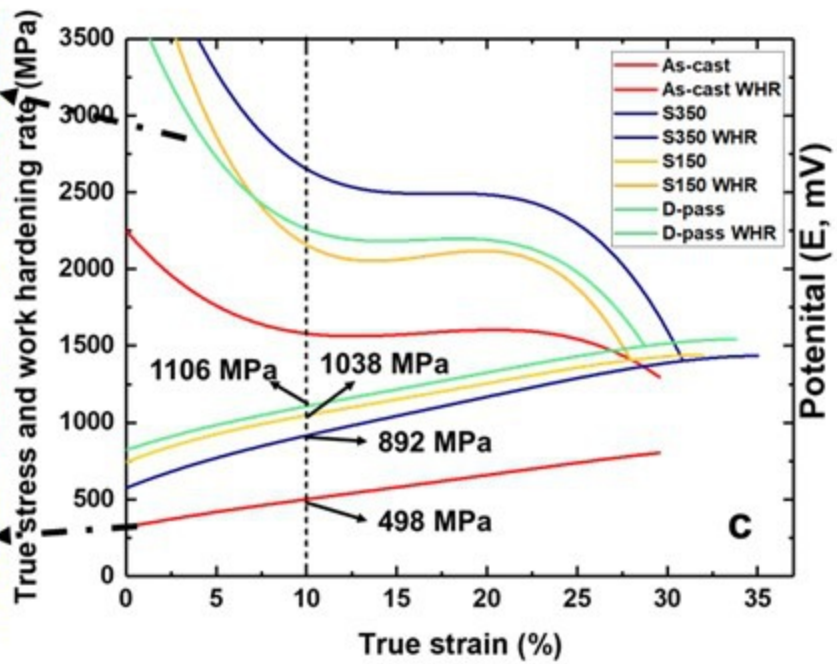

Strength-ductility synergy

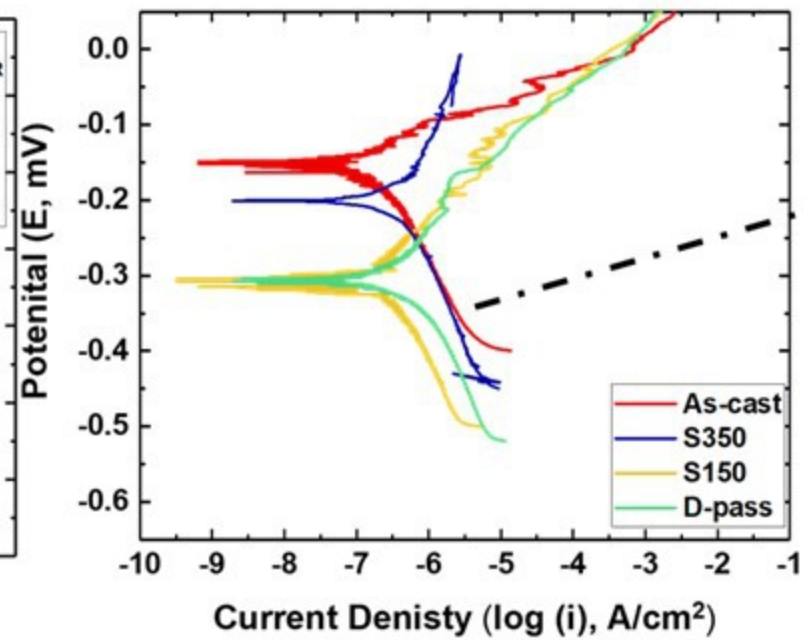
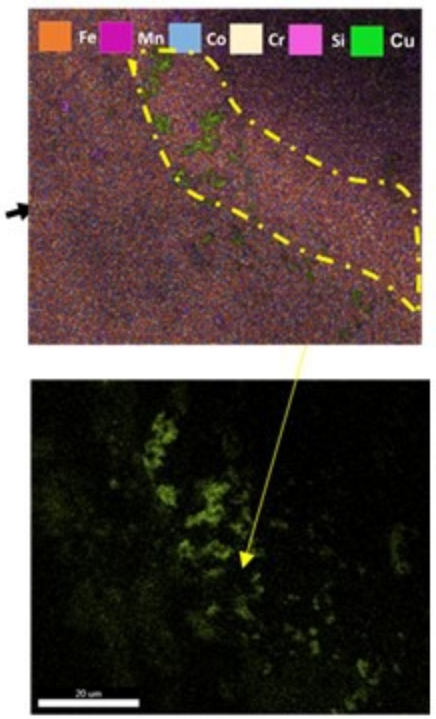
Corrosion Resistance